



Optical and thermal properties of $\text{Ge}_2\text{Sb}_2\text{Te}_5$, Sb_2Se_3 , and Sb_2S_3 for reconfigurable photonic devices [Invited]

KIUMARS ARYANA,^{1,8}  HYUN JUNG KIM,^{1,9}  MD. RAFIQUL ISLAM,²  NINA HONG,³  COSMIN-CONSTANTIN POPESCU,⁴  SARA MAKAREM,²  TIAN GU,^{4,5}  JUEJUN HU,^{4,5}  AND PATRICK E. HOPKINS^{2,6,7} 

¹NASA Langley Research Center, Hampton, VA 23666, USA

²Department of Mechanical and Aerospace Engineering, University of Virginia, Charlottesville, VA 22904, USA

³J.A. Woollam Co., Inc, Lincoln, NE 68508, USA

⁴Department of Materials & Science Engineering, Massachusetts Institute of Technology, Cambridge, MA, USA

⁵Materials Research Laboratory, Massachusetts Institute of Technology, Cambridge, MA, USA

⁶Department of Materials Science and Engineering, University of Virginia, Charlottesville, VA 22904, USA

⁷Department of Physics, University of Virginia, Charlottesville, VA 22904, USA

⁸kiumars.aryana@nasa.gov

⁹hyunjung.kim@nasa.gov

Abstract: Phase change materials (PCMs) are one of the most promising materials candidates for reconfigurable optics owing to their two solid-state atomic structures that render distinct optical properties. Recently, there have been growing interests in integrating these materials into photonic devices for achieving reconfigurable optical properties. In this paper, we focus on examining the optical and thermal properties of three essential phase change materials: $\text{Ge}_2\text{Sb}_2\text{Te}_5$, Sb_2Se_3 , and Sb_2S_3 . The latter two have been specifically tailored for photonic applications, with minimal absorption losses in the near-infrared spectrum. In particular, we report the optical constants, refractive index (n) and extinction coefficient (k), for 300 nm thick $\text{Ge}_2\text{Sb}_2\text{Te}_5$, Sb_2Se_3 , and Sb_2S_3 on CaF_2 substrate across a wide spectral range of 0.3 μm to 40 μm in amorphous and crystalline states. We observe that while $\text{Ge}_2\text{Sb}_2\text{Te}_5$ exhibits a larger contrast in the index of refraction upon phase transformation compared to the other two compositions, Sb_2Se_3 and Sb_2S_3 demonstrate a substantial reduction in their extinction coefficients within the infrared spectrum. In addition, using time-domain thermorefectance (TDTR), we report their thermal conductivity as a function of temperature up to 320°C. According to our observation, the room temperature thermal conductivity of Sb_2Se_3 and Sb_2S_3 increases by almost a factor of four upon phase transformation from amorphous to crystalline. The findings of this study provides necessary parameters for modeling PCM based photonic devices and emphasize the strong potential of Sb_2Se_3 and Sb_2S_3 as promising material candidates for reconfigurable optics due to their low-loss transmission in infrared spectrum, paving the way for their practical implementation in future photonic devices.

© 2023 Optica Publishing Group under the terms of the [Optica Open Access Publishing Agreement](#)

1. Introduction

Photonic systems have become an indispensable part of the modern technology from information processing to autonomous vehicle and biological sensing/imaging [1–4]. The momentum to complement electronic integrated circuits with photonic components has gained significant traction in recent years, driven by the exceptional properties they offer such as higher speeds,

broader bandwidths, low-loss transmission, and reduced power consumption [5–7]. For many of the applications, it is crucial to develop materials and technologies that enable reliable manipulation of light on solid-state chips and are compatible with standard semiconductor fabrication processes. To date, for modulating electromagnetic waves, a number of different techniques have been implemented including electro-optical [8], magneto-optical [9,10], thermo-optical [11,12], opto-mechanical [13], and acousto-optical [14] effects. Nonetheless, there remains a significant need for more efficient non-mechanical adaptive technologies that can manipulate the wavefront of light with high-speed and a robust mechanism.

Chalcogenide-based phase change materials (PCMs) have recently received considerable attention for application in reconfigurable photonics due to their large contrasting properties between their amorphous and crystalline atomic structures [15]. The switching mechanism in PCMs can be exceptionally rapid, reaching tens of nanoseconds speeds [16], which is triggered by thermal excitation. Unlike liquid crystals and piezoelectric tuning systems, PCMs possess a non-volatile nature and once switched, no energy is required to maintain the PCM in their respective state. The most widely used PCM, $\text{Ge}_2\text{Sb}_2\text{Te}_5$, has been proven as a successful material candidate for applications in data storage owing to the large electrical resistivity contrast—five orders of magnitude—between its two solid-state phases [17]. However, this composition is primarily optimized for storage and memory applications. To broaden the scope of PCMs and enable their application in more diverse technologies, it is crucial to customize their properties with respect to their target application to achieve optimal efficiency. For instance, in transmissive optics such as zoom lenses and optical filters, it is important for the PCM to exhibit low absorption in both phases while possessing a large contrast in its refractive index between the two phases. In addition, as with any other materials, PCMs behave differently depending on the operating wavelength, and therefore, it is crucial to select a PCM with respect to the required wavelength spectrum. For instance, $\text{Ge}_2\text{Sb}_2\text{Te}_5$ is highly absorptive in the visible and near-IR range due to photon energy above bandgap with relatively small change in the refractive index. This high absorption primarily stems from the fact that Tellurium (Te) is an element with a small bandgap, 0.35 eV [18].

Several endeavors have been made to replace Te with Selenium (Se) due to its significantly larger bandgap, approximately 1.8 eV, which leads to lower absorption for wavelength energies closer to the visible spectrum [19–24]. Recently, quaternary alloy $\text{Ge}_2\text{Sb}_2\text{Se}_4\text{Te}$ (GSST) has received a great deal of attention due to its phase stability and low loss property in the crystalline phase for near-IR and mid-IR ranges [22,25]. However, this composition is still optically lossy in the visible and near-IR spectrum [26]. Considering this, Te-free binary alloys such as Sb_2S_3 and Sb_2Se_3 are more favorable and have shown to be less absorptive in the near-IR and even visible spectrum [23,24]. In addition, owing to the presence of fewer elements in these binary alloys, it is anticipated that the materials exhibit a higher thermal conductivity than GSST, which is crucial for a more uniform distribution of temperature in the PCM upon cycling [27].

Extensive efforts have been dedicated to precisely tailoring the properties of PCMs to enhance the efficiency of photonic devices [28]. Sb_2S_3 and Sb_2Se_3 have shown great potentials for tuning light at near-IR spectrum. To the best of our knowledge, this study is the first to report optical constants, refractive index and extinction coefficient, for Sb_2S_3 and Sb_2Se_3 across a wide spectral range of 0.3 μm to 40 μm . In addition, we quantified the thermal conductivity of Sb_2S_3 and Sb_2Se_3 across different annealing temperatures, from room temperature up to 320°C. For comparison, we measure the same properties for GST that is fabricated through the same deposition technique. These optical and thermal parameters are critical to designing low-loss photonic devices using both photothermal and electrothermal switching schemes.

2. Fabrication

For this study, we deposited various thin films of PCMs, specifically GST, Sb_2Se_3 , and Sb_2S_3 , with a nominal thickness of 300 nm onto CaF_2 and silicon substrates for characterizing their optical and thermal properties, as shown in Fig. 1. For testing optical properties, double-side polished 1.5×25.4 mm (1-inch optics) CaF_2 wafers (witness sample / Esco PN: W1410T, Esco Optics, Inc.) were sonicated in acetone, iso-propanol, and deionized water sequentially, twice, followed by an ultrahigh purity compressed nitrogen (N_2) blow dry, before deposition. For testing the thermal properties, $50.8 \text{ mm} \pm 0.2 \text{ mm}$ (2-inch) diameter, single-side polished, $\langle 100 \rangle$ N-type silicon wafers (University wafer Inc.) were prepared after the same cleaning procedure of the CaF_2 wafers. Three separate 3-inch diameter sputtering targets were used for the chalcogenide films: Sb_2S_3 (Antimony Sulfide, 99.95% purity, American Elements), Sb_2Se_3 (Antimony Selenide, 99.95% purity, Kurt J. Lesker) and $\text{Ge}_2\text{Sb}_2\text{Te}_5$ target (14.3 wt% Ge, 23.8 wt% Sb, 61.9 wt% Te, Mitsubishi Materials, Inc.). The targets were 3-inch diameter and 0.250-inch thickness including 0.125-inch thickness indium back bonding.

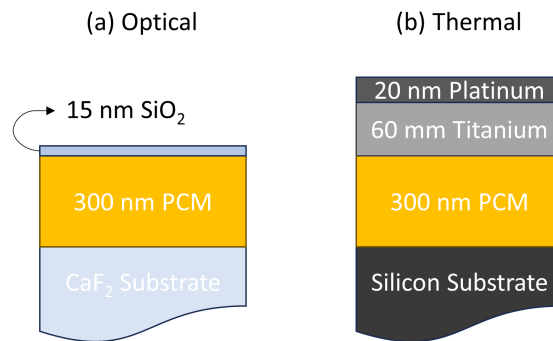


Fig. 1. Schematic showing layers configuration for measuring (a) optical properties, and (b) thermal properties.

All thin-films were deposited via 100 W RF magnetron sputtering at a base pressure of 2.6×10^{-7} Torr and a deposition pressure of 5 mTorr (40 sccm Ar flow, research-grade, 99.9999% purity). The deposition rates of $\text{Ge}_2\text{Sb}_2\text{Te}_5$, Sb_2S_3 , and Sb_2Se_3 are 1.84 nm / sec., 1.49 nm / sec., 1.86 nm / sec., respectively from the step scanning between the film and the wafer using profilometer (VEECO WYKO NT9100 Optical Profilometer). For the 300 nm films, GST, Sb_2S_3 , and Sb_2Se_3 were deposited for 10 min 2 sec., 12 min, and 10 min. 11 sec., respectively. The chemical composition of as-deposited GST thin-films was determined by DCP-AES (Direct Current Plasma-Atomic Emission Spectroscopy, Luvak, Inc.). The composition was measured as 22 at% Ge, 23.5 at% Sb, and 54.5 at% Te, which is close to a nominal composition of bulk $\text{Ge}_{22.2}\text{Sb}_{22.2}\text{Te}_{55.6}$.

3. Results

In order to measure the optical properties of PCMs across their various structural phases, i.e. fully amorphous, partial-crystalline, and fully crystalline, the samples were annealed at different temperatures. To prevent oxidation at elevated temperatures, a 15 nm layer of SiO_2 was deposited on the samples as a protective capping layer. After protective layer deposition, the samples were placed at the center of a programmable hot plate and heated up to 200, and 300°C with a ramp rate of 200°C/hr. They were kept for an hour at each specified temperature and cooled down by turning the heater off under ambient condition.

Figure 2 shows qualitative images of each sample using a visible camera before and after annealing at 200°C and 300°C. According to these images, the CaF_2 substrate does not show any

noticeable variation at different annealing temperatures. We also confirm this by performing Fourier Transform Infrared (FTIR) spectroscopy, which reveals no discernible change in the transmission spectra of the substrate upon annealing. In the case of GST, its opacity in the visible spectrum precludes the detection of any changes through the use of a visible camera. On the other hand, as evident in Fig. 2, the as-deposited amorphous phase of Sb_2Se_3 and Sb_2S_3 exhibits some level of transparency, particularly in the higher end of the visible spectrum. One notable difference is the transmitted color in the case of Sb_2Se_3 and Sb_2S_3 . From previous studies, we know the bandgaps for Sb_2Se_3 and Sb_2S_3 in the amorphous phase are 1.56 eV (795 nm) and 2.05 eV (605 nm), respectively [23,29]. In Fig. 2, our observations are consistent with this, as we clearly witness the transmission of only red light through the Sb_2Se_3 samples and yellowish light through the Sb_2S_3 samples. Upon annealing, the bandgaps of all PCMs shrink which are listed in Table 1 and as a result, the material absorbs light at lower energies and subsequently blocking any visible light from transmitting through. This is evident in Fig. 2, where upon annealing to 200°C, we observe that Sb_2Se_3 loses its transparency in red and become completely opaque, while Sb_2S_3 remains unaltered. This is related to the higher crystallization temperature of Sb_2S_3 , which is near ~250°C according to previous studies [24,30]. We confirm this by annealing Sb_2S_3 at 300°C, where we observe a color change in the transmitted light. It becomes evident that only red light is transmitted, serving as an indication of going under a phase transformation.

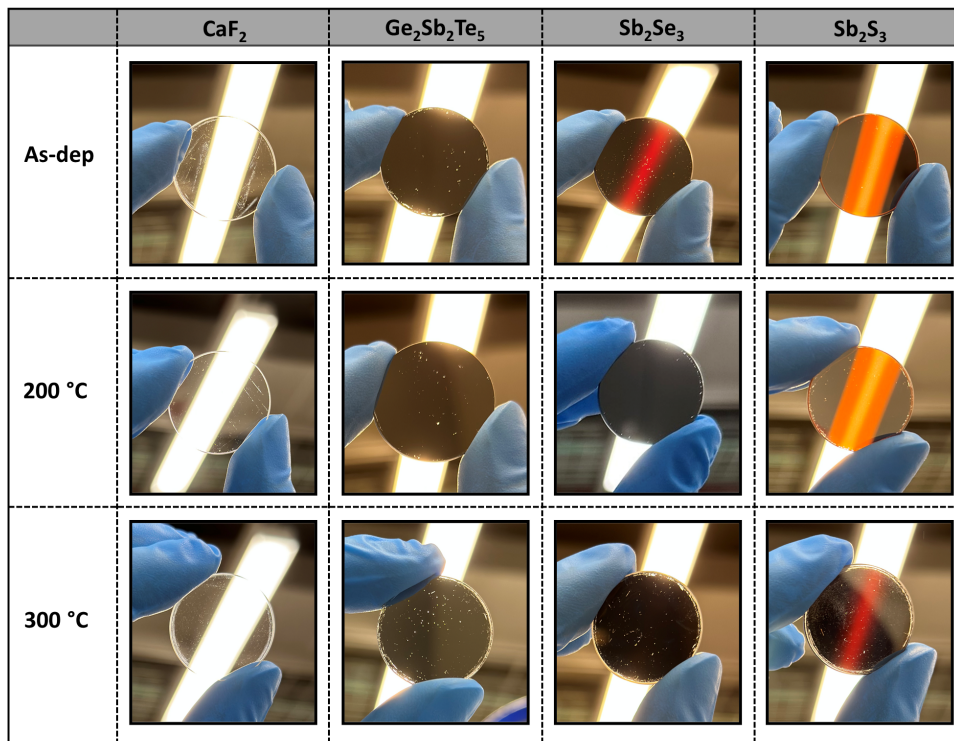


Fig. 2. Qualitative images of PCM thin films on CaF_2 substrate at various annealing temperatures, captured using a visible camera.

In order to quantify the optical properties of the PCMs studied here, we measure their refractive index (n) and extinction coefficient (k). The film thickness and optical constants of $\text{Ge}_2\text{Sb}_2\text{Te}_5$, Sb_2Se_3 , and Sb_2S_3 films capped with a thin SiO_2 layer have been evaluated at different annealing temperatures in a wide spectral range from 300 nm to 40000 nm using the J.A. Woollam M-2000 (from 300 nm to 1700 nm) and IR-VASE Mark II (from 1700 nm to 40000 nm) spectroscopic

ellipsometers. Both ellipsometers are rotating compensator-based, enabling phase measurement in the full range without ambiguity. This is ideal for samples grown on a transparent substrate. The data from both ellipsometers were analyzed simultaneously with a single Kramers-Kronig consistent model.

The optical constants of CaF₂ wafer and SiO₂ capping layer were predetermined using pristine samples, and they are held fixed in the models for the PCMs. The absorption by electronic transitions in the UV-VIS range of all PCMs was modeled using a Tauc-Lorentz oscillator along with one or more Gaussian oscillators. Both Ge₂Sb₂Te₅ and Sb₂Se₃ films in their as-deposited amorphous phase exhibit good transparency in the mid-IR range. Annealing and crystallization lead to strong near-IR absorption in Ge₂Sb₂Te₅ due to significant free carrier absorption in the mid-IR. In comparison, the optical absorption is much smaller in Sb₂Se₃. On the other hand, we observed that the mid-IR absorption in Sb₂S₃ can be modeled using a Drude oscillator, indicating presence of free carrier absorption. This might be a consequence of slight stoichiometric deviations, or impurities.

Figure 3 shows the optical constants, n & k , values for Ge₂Sb₂Te₅, Sb₂Se₃, and Sb₂S₃ in as-deposited amorphous phase as well as after annealing at 200°C and 300°C for 1 hour. It is worth noting that, as anticipated, due to the higher crystallization temperature of Sb₂S₃, the other two compositions are crystallized at 200°C, whereas Sb₂S₃ only crystallizes at 300°C. To facilitate comparison between different compositions, we have selected a reference wavelength of 1550 nm, which is indicated on the plot using a dashed line. According to Fig. 3(a) the refractive index of GST increases by 2.7 upon amorphous to crystalline phase transformation. Similarly, the extinction coefficient, which directly correlates with absorption losses, rises from 0.08 to 1.23. This large increase in the extinction coefficient results in high absorption losses within the crystalline phase, making GST unsuitable for use in transmissive optics such as reconfigurable lenses or beam steering devices. In the case of Sb₂Se₃, even though the refractive index exhibits a modest increase of 0.74, which is notably lower compared to GST, the extinction coefficients in both the amorphous and the crystalline phases are markedly lower than those of GST. This characteristic makes Sb₂Se₃ a highly suitable choice for low-loss transmissive optics. Similarly, in the case of Sb₂S₃, the change in refractive index upon phase transformation is closer to 0.90, slightly larger than that observed in Sb₂Se₃. However, the extinction coefficient for Sb₂S₃ also experiences a greater increase. Consequently, this suggests that the Sb₂S₃ composition is expected to exhibit a higher degree of absorption than Sb₂Se₃ at this specific wavelength. This observation may appear surprising, given that Sb₂S₃ has a larger bandgap and is expected to exhibit lower absorption losses. While we lack a compelling explanation for this observation, it is

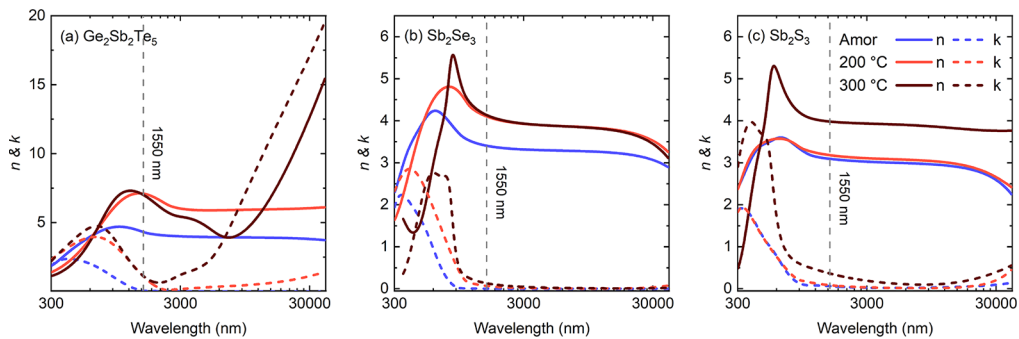


Fig. 3. Spectroscopic refractive index (n) represented by solid lines, and the extinction coefficient (k) represented by dashed lines, for 300 nm thick PCMs (a) Ge₂Sb₂Te₅, (b) Sb₂Se₃, and (c) Sb₂S₃ at various annealing temperatures. For the sake of comparison, a vertical dashed line has been included at 1550 nm on each plot.

worth noting that this larger absorption could potentially result from an unoptimized composition or long annealing times.

4. Thermal conductivity

Time-domain thermoreflectance (TDTR) was employed to measure the thermal conductivity of thin film PCMs. TDTR is a pump-probe thermometry technique that utilizes ultrashort laser pulses (<picosecond) to induce localized heating and by detecting the subsequent thermal decay in the materials, it allows us to extract their thermal properties. In this technique the output of a Ti:sapphire oscillator at repetition rate of 80 MHz centered at 808 nm was split into a high energy pump path and a low energy probe path. The pump beam is modulated at 8.4 MHz to create oscillatory heating events on the surface of the sample, allowing the heat to diffuse to underneath layers. After passing through a 10X focusing objective, pump and probe are focused down to 20 and 10 μm , respectively. Depending on the thermal properties of the underlying layers such as thermal conductivity, heat capacity, and thickness, the transient temperature decay curve changes. We can detect this temperature decay with sub-picosecond resolution using the probe beam that is mechanically delayed in time with respect to the pump pulse. By experimentally measuring the temperature decay curve and fitting our thermal model that solves the heat diffusion equation, we can extract properties such as thermal boundary conductance and thermal conductivity of the underlying layers.

In TDTR, achieving accurate measurements of the changes in the temperature of the surface necessitates coating the sample with a metallic layer of approximately 80 nm thickness. This metallic layer serves as the transducer, which facilitates the detection of temperature changes on the sample's surface. Aluminum is commonly used as the transducer due to its ubiquity and high thermo-reflectance coefficient, dR/dT , at the probe wavelength (808 nm). However, it is noted that aluminum exhibits instability at elevated temperatures, and our observations indicate delamination occurring near 300°C. Similarly, we observe the same behavior for Pt at temperatures around 300°C. We attribute this to the absence of a diffusion barrier between the PCM and the metallic transducer. To resolve this, we used 60nm-thick titanium (Ti) with 20nm-thick platinum (Pt) as the transducer, and was able to successfully measure the thermal conductivity of PCM up to 320°C without any sign of delamination.

To ensure the accuracy of our thermal conductivity measurements as a function of temperature for the Pt/Ti transducer, we performed a calibration test using a sapphire (Al_2O_3) substrate and GST thin film on silicon substrate. The purpose of this calibration test was to establish a reliable baseline for our subsequent thermal conductivity measurements. For measuring thermal conductivity at elevated temperature, we employed a temperature control stage (Linkam HFS600E-PB4), while flowing Argon to minimize oxidation. For thermal analysis, we assumed a 3-layer and 4-layer model for the sapphire (Pt/Ti/sapphire) and GST thin film (Pt/Ti/GST/Si), respectively. The parameters used in our thermal model is given in Table 1. The thermal conductivity for the Pt and Ti transducer were assumed to be 25 and 17 W m K^{-1} , respectively [31,32]. We use the temperature-dependant heat capacity for Pt from Ref. [33] and assumed a constant volumetric heat capacity of 2.36 $\text{MJ m}^{-3} \text{K}^{-1}$ for Ti layer.

Figure 4(a) shows the thermal conductivity of sapphire as a function of temperature up to 320°C. For this analysis, we fit for the interfacial thermal conductance between Ti and PCM, $G_{\text{Ti}/\text{PCM}}$, and thermal conductivity of the sapphire, $k_{\text{Al}_2\text{O}_3}$. The measured thermal conductivity agrees very well with literature value. To verify that no permanent changes occurred in the sample as a result of heating, we also measured its thermal conductivity upon returning the sample back to room temperature. As can be seen, the star symbol perfectly aligns with the pre-heating measurement, affirming the repeatability of our experimental results. This alignment provides confidence that the sample retained its original properties after the heating process.

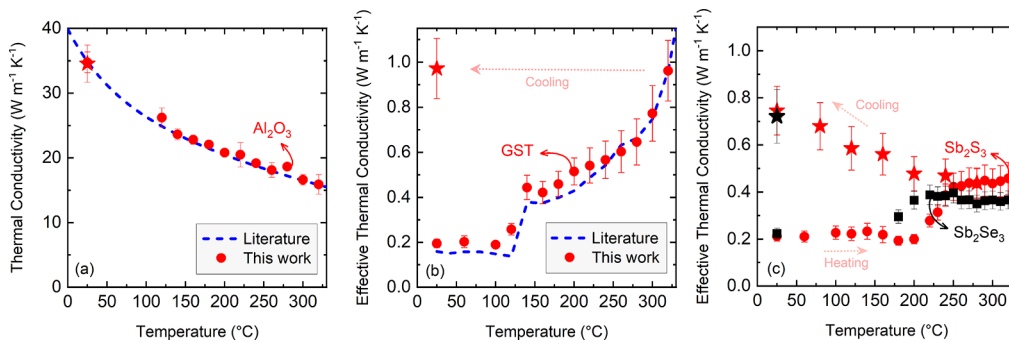


Fig. 4. Thermal conductivity versus temperature for (a) Al_2O_3 and (b) GST, compared to literature values [34,35]. Panel (c) shows measured thermal conductivities for Sb_2Se_3 and Sb_2S_3 . The uncertainty for (a) is standard deviation across the scans at different locations on the samples and for (b & c) are calculated based on 10% deviation in the volumetric heat capacity of the PCM.

Figure 4(b) shows the thermal conductivity of 300 nm GST on a silicon substrate. In this analysis, we made the assumption that the interfacial thermal resistance between all layers were infinite. While this assumption may be reasonable for PCMs in their amorphous phase due to its low thermal conductivity, it becomes more critical to consider the interfacial thermal resistance as they transition to a crystalline state with higher thermal conductivity [36,37]. Although interfacial thermal resistance is less of a concern for the large thickness that studied here, to account for the sensitivity to the effect of boundaries, we report the effective thermal conductivity, which signifies that the reported value includes the impact of interfaces. In other words, we assume the interfacial thermal resistance is zero and fit for the thermal conductivity of Ti and PCM layer. Consequently, any effect arising from interfacial thermal resistance is incorporated within the reported thermal conductivity values. As a result, it is possible that the intrinsic thermal conductivity of the PCMs may be slightly higher than the values currently reported in this study. Furthermore, considering the significant variation in the literature regarding the heat capacity of the PCMs, and to ensure consistency in our study, we adopt the heat capacity values corresponding to the crystalline phase, which are more readily available. To account for the uncertainty, we calculated the uncertainty based on a $\pm 10\%$ deviation margin in the heat capacity. From this, the measured thermal conductivity of GST agrees well with prior thermal conductivity measurements [35,38]. The strong agreement between our measurements in this study and the values reported in the literature for sapphire and GST validates the accuracy of our assumptions and the reliability of our results for both Sb_2Se_3 and Sb_2S_3 . It must be mentioned that in our thermal conductivity measurements, we observe a systematic reduction in the thermal conductivity of Ti in samples containing PCM at temperatures above 200 C. We attribute this reduction to the interaction between Ti and the PCM elements at the interface [39–41].

Using the same measurement configuration and analysis, the thermal conductivity of Sb_2Se_3 and Sb_2S_3 as a function of temperature are presented in Fig. 4(c). In the amorphous phase, the thermal conductivity values for Sb_2Se_3 and Sb_2S_3 were measured at 0.22 and 0.21 $\text{W m}^{-1} \text{K}^{-1}$, respectively, showing great agreement with recent measurements on 40 nm Sb_2S_3 [42]. As can be seen in Fig. 4(c), the thermal conductivity of Sb_2S_3 stays relatively constant up to 200°C and reaches a maximum of 0.45 $\text{W m}^{-1} \text{K}^{-1}$ at 250°C . In the case of Sb_2Se_3 , we measure the sample at room temperature and heat the sample up to 180°C right before its crystallization temperature. We can see that the thermal conductivity starts to increase from 180°C and reaches a maximum of 0.36 $\text{W m}^{-1} \text{K}^{-1}$ at 220°C and stays relatively constant up to 320°C . One notable observation here is that when the samples were returned to room temperature, indicated by the

star symbol, the thermal conductivity of Sb_2Se_3 and Sb_2S_3 increased to 0.72 and $0.74 \text{ W m}^{-1} \text{ K}^{-1}$, respectively, representing nearly 100% and 64% increase in their thermal conductivity upon cooling. In order to ensure the accuracy of the results presented here, we measured the thermal conductivity of crystalline Sb_2S_3 upon cooling. Our observations show a continuous increase, from 0.45 at 320°C to $0.74 \text{ W m}^{-1} \text{ K}^{-1}$ at room temperature.

The measured room temperature thermal conductivity at crystalline phase is higher than the previously reported values [42]. The discrepancy may arise from variations in the assumed heat capacity, as well as the differing thicknesses of the films under study, which directly contribute to an increased influence of interfacial thermal resistance, particularly noticeable in thinner films approaching 40 nm . In a prior study [43] with thicknesses comparable to those examined in Ref. [42], it was shown that interfacial thermal resistance could decrease the effective thermal conductivity of GST in the crystalline phase by up to a factor of four for a 20 nm film and a factor of two for 40 nm films. In addition, the observed increase in thermal conductivity at lower temperatures aligns with our understanding of diffuse thermal transport in crystals. From a microscopic viewpoint of thermal transport, the scattering of phonons due to anharmonic effects reduces at lower temperatures. Consequently, in ordered materials, we anticipate a higher thermal conductivity at lower temperatures, similar to the behavior seen in the sapphire measurement in Fig. 4(a).

Table 1. Room temperature optical and thermal properties of PCMs investigated in this study. The thermal conductivity values provided for the PCMs' crystalline phase are based on annealing at temperature of 320°C .

PCM	Phase	Thickness (nm)	Specific Heat ($\text{J kg}^{-1} \text{ K}^{-1}$)	Density (kg m^{-3})	Thermal Conductivity ($\text{W m}^{-1} \text{ K}^{-1}$)	Optical Bandgap (eV)
$\text{Ge}_2\text{Sb}_2\text{Te}_5$	amorphous	302	221 [43,44]	5870 [45]	0.20	0.74 [46]
	crystalline	280	223 [43,44]	6270 [45]	1.02	0.50 [46]
Sb_2Se_3	amorphous	346	N/A	N/A	0.22	1.56 [29]
	crystalline	312	263 [47]	5840 [48]	0.72	1.17-1.27 [29,48]
Sb_2S_3	amorphous	275	N/A	4150 [49]	0.21	2.05 [23]
	crystalline	241	368 [50,51]	4640 [49]	0.74	1.72 [23]

5. Conclusion

In this study, we examined the optical and thermal properties of three popular phase change materials for photonic applications, namely $\text{Ge}_2\text{Sb}_2\text{Te}_5$, Sb_2Se_3 , and Sb_2S_3 . We demonstrated how their optical constants and thermal conductivity changes upon phase transformation from amorphous to crystalline. Both Sb_2Se_3 and Sb_2S_3 display less contrast in their refractive indices compared to GST. Yet, they also possess notably lower extinction coefficients in their crystalline phases, making them highly suitable candidates for reconfigurable transmissive optics. It is essential to acknowledge that the results presented here pertain to films with relatively large thicknesses (300 nm). Additionally, according to our thermal conductivity measurements, we observed that the thermal conductivity of Sb_2S_3 and Sb_2Se_3 are more than a factor of two lower than that of GST at 320°C . We observed that the thermal conductivity of Sb_2Se_3 and Sb_2S_3 increases to 0.72 and $0.74 \text{ W m}^{-1} \text{ K}^{-1}$ at room temperature, which is almost a factor two increase compared to their thermal conductivity at elevated temperature (320°C). The results presented here would pave the way for designing future PCM-based reconfigurable optics.

6. Disclaimer

Specific vendor and manufacturer names are explicitly mentioned only to accurately describe the test hardware. The use of vendor and manufacturer names does not imply an endorsement by the U.S. Government nor does it imply that the specified equipment is the best available.

Funding. Air Force Office of Scientific Research (FA9550-22-1-0456).

Acknowledgements. This work was partially supported by the Air Force Office of Scientific Research, Grant Number FA9550-22-1-0456. This research was sponsored by the National Aeronautics and Space Administration (NASA) through a contract with ORAU. The views and conclusions contained in this document are those of the authors and should not be interpreted as representing the official policies, either expressed or implied, of the National Aeronautics and Space Administration (NASA) or the U.S. Government. The U.S. Government is authorized to reproduce and distribute reprints for Government purposes notwithstanding any copyright notation herein.

Disclosures. The authors declare no competing interests.

Data availability. The data that support the findings of this study are available from the corresponding author upon reasonable request.

References

1. R. Chandrasekar, Z. J. Lapin, A. S. Nichols, R. M. Braun, and A. W. Fountain III, "Photonic integrated circuits for department of defense-relevant chemical and biological sensing applications: state-of-the-art and future outlooks," *Opt. Eng.* **58**(02), 1 (2019).
2. B. J. Shastri, A. N. Tait, and T. Ferreira de Lima, *et al.*, "Photonics for artificial intelligence and neuromorphic computing," *Nat. Photonics* **15**(2), 102–114 (2021).
3. N. Quack, A. Y. Takabayashi, and H. Sattari, *et al.*, "Integrated silicon photonic mems," *Microsyst. Nanoeng.* **9**(1), 27 (2023).
4. H. J. Kim, S. Borg, and S. Bartram, *et al.*, "P-active project report," *NASA Technical Reports Server* (2023).
5. D. A. Miller, "Attojoule optoelectronics for low-energy information processing and communications," *J. Lightwave Technol.* **35**(3), 346–396 (2017).
6. H. Guillet de Chatellus, L. Romero Cortés, C. Schnébelin, M. Burla, and J. Aza na, "Reconfigurable photonic generation of broadband chirped waveforms using a single cw laser and low-frequency electronics," *Nat. Commun.* **9**(1), 2438 (2018).
7. J. Feldmann, N. Youngblood, and M. Karpov, *et al.*, "Parallel convolutional processing using an integrated photonic tensor core," *Nature* **589**(7840), 52–58 (2021).
8. Q. Xu, B. Schmidt, S. Pradhan, and M. Lipson, "Micrometre-scale silicon electro-optic modulator," *Nature* **435**(7040), 325–327 (2005).
9. L. D. Tzuang, K. Fang, P. Nussenzeig, S. Fan, and M. Lipson, "Non-reciprocal phase shift induced by an effective magnetic flux for light," *Nat. Photonics* **8**(9), 701–705 (2014).
10. H. Takagi, K. Nakamura, T. Goto, P. Lim, and M. Inoue, "Magneto-optic spatial light modulator with submicron-size magnetic pixels for wide-viewing-angle holographic displays," *Opt. Lett.* **39**(11), 3344–3347 (2014).
11. N. C. Harris, Y. Ma, and J. Mower, *et al.*, "Efficient, compact and low loss thermo-optic phase shifter in silicon," *Opt. Express* **22**(9), 10487–10493 (2014).
12. M. Bosch, M. Shcherbakov, Z. Fan, and G. Shvets, "Polarization states synthesizer based on a thermo-optic dielectric metasurface," *J. Appl. Phys.* **126**(7), 073102 (2019).
13. E. Arbabi, A. Arbabi, and S. M. Kamali, *et al.*, "Mems-tunable dielectric metasurface lens," *Nat. Commun.* **9**(1), 812 (2018).
14. Z. Sun, A. Martinez, and F. Wang, "Optical modulators with 2D layered materials," *Nat. Photonics* **10**(4), 227–238 (2016).
15. S. Abdollahramezani, O. Hemmatyar, and H. Taghinejad, *et al.*, "Tunable nanophotonics enabled by chalcogenide phase-change materials," *Nanophotonics* **9**(5), 1189–1241 (2020).
16. Y. Zhang, C. Ríos, and M. Y. Shalaginov, *et al.*, "Myths and truths about optical phase change materials: A perspective," *Appl. Phys. Lett.* **118**(21), 210501 (2021).
17. H.-S. P. Wong, S. Raoux, and S. Kim, *et al.*, "Phase change memory," *Proc. IEEE* **98**(12), 2201–2227 (2010).
18. I. Hadar, X. Hu, Z.-Z. Luo, V. P. Dravid, and M. G. Kanatzidis, "Nonlinear band gap tunability in selenium–tellurium alloys and its utilization in solar cells," *ACS Energy Lett.* **4**(9), 2137–2143 (2019).
19. S. Buller, C. Koch, and W. Bensch, *et al.*, "Influence of partial substitution of te by se and ge by sn on the properties of the blu-ray phase-change material ge₈sb₂te₁₁," *Chem. Mater.* **24**(18), 3582–3590 (2012).
20. E. Vinod, K. Ramesh, and K. Sangunni, "Structural transition and enhanced phase transition properties of se doped ge₂sb₂te₅ alloys," *Sci. Rep.* **5**(1), 8050 (2015).
21. R. Svoboda and J. Málek, "Amorphous-to-crystalline transition in te-doped ge₂sb₂se₅ glass," *J. Therm. Anal. Calorim.* **117**(3), 1073–1083 (2014).
22. Y. Zhang, J. B. Chou, and J. Li, *et al.*, "Broadband transparent optical phase change materials for high-performance nonvolatile photonics," *Nat. Commun.* **10**(1), 4279 (2019).

23. W. Dong, H. Liu, and J. K. Behera, *et al.*, “Wide bandgap phase change material tuned visible photonics,” *Adv. Funct. Mater.* **29**(6), 1806181 (2019).
24. M. Delaney, I. Zeimpekis, D. Lawson, D. W. Hewak, and O. L. Muskens, “A new family of ultralow loss reversible phase-change materials for photonic integrated circuits: Sb_2S_3 and Sb_2Se_3 ,” *Adv. Funct. Mater.* **30**(36), 2002447 (2020).
25. C.-C. Popescu, S. Vitale, and C. Roberts, *et al.*, “Learning from failure: boosting cycling endurance of optical phase change materials,” In *Photonic and Phononic Properties of Engineered Nanostructures XIII*, vol. 12431, 40–48 (SPIE, 2023).
26. C.-C. Popescu, K. P. Dao, and L. Ranno, *et al.*, “An open-source multi-functional testing platform for optical phase change materials,” *arXiv*, arXiv:2307.06216 (2023).
27. K. Aryana, H. J. Kim, and C.-C. Popescu, *et al.*, “Toward accurate thermal modeling of phase change material based photonic devices,” *arXiv* arXiv:2305.14145 (2023).
28. B. J. Kooi and M. Wuttig, “Chalcogenides by design: Functionality through metavalent bonding and confinement,” *Adv. Mater.* **32**(21), 1908302 (2020).
29. P. Singh, N. Ghorai, A. Thakur, and H. N. Ghosh, “Temperature-dependent ultrafast charge carrier dynamics in amorphous and crystalline sb_2se_3 thin films,” *J. Phys. Chem. C* **125**(9), 5197–5206 (2021).
30. M. Kassem, C. J. Benmore, and A. Tverjanovich, *et al.*, “Glassy and liquid sb_2s_3 : insight into the structure and dynamics of a promising functional material,” *J. Mater. Chem. C* **11**(14), 4654–4673 (2023).
31. X. Zhang, H. Xie, and M. Fujii, *et al.*, “Thermal and electrical conductivity of a suspended platinum nanofilm,” *Appl. Phys. Lett.* **86**(17), 171912 (2005).
32. D. Thuau, I. Koymen, and R. Cheung, “A microstructure for thermal conductivity measurement of conductive thin films,” *Microelectron. Eng.* **88**(8), 2408–2412 (2011).
33. H. Yokokawa and Y. Takahashi, “Laser-flash calorimetry ii. heat capacity of platinum from 80 to 1000 k and its revised thermodynamic functions,” *J. Chem. Thermodyn.* **11**(5), 411–420 (1979).
34. D. G. Cahill, S.-M. Lee, and T. I. Selinder, “Thermal conductivity of $\kappa\text{-al}_2\text{o}_3$ and $\alpha\text{-al}_2\text{o}_3$ wear-resistant coatings,” *J. Appl. Phys.* **83**(11), 5783–5786 (1998).
35. K. Aryana, Y. Zhang, and J. A. Tomko, *et al.*, “Suppressed electronic contribution in thermal conductivity of $\text{Ge}_2\text{Sb}_2\text{Se}_4\text{Te}$,” *Nat. Commun.* **12**(1), 1–9 (2021).
36. K. Aryana, D. A. Stewart, and J. T. Gaskins, *et al.*, “Tuning network topology and vibrational mode localization to achieve ultralow thermal conductivity in amorphous chalcogenides,” *Nat. Commun.* **12**(1), 2817 (2021).
37. M. S. B. Hoque, Y. R. Koh, and K. Aryana, *et al.*, “Thermal conductivity measurements of sub-surface buried substrates by steady-state thermoreflectance,” *Rev. Sci. Instrum.* **92**(6), 1 (2021).
38. H.-K. Lyeo, D. G. Cahill, and B.-S. Lee, *et al.*, “Thermal conductivity of phase-change material $\text{ge}_2\text{sb}_2\text{te}_5$,” *Appl. Phys. Lett.* **89**(15), 151904 (2006).
39. S. Loubriat, D. Muyard, and F. Fillot, *et al.*, “GeTe phase change material and Ti based electrode: Study of thermal stability and adhesion,” *Microelectronic Engineering* **88**(5), 817–821 (2006).
40. D. Gao, B. Liu, and Z. Xu, *et al.*, “The Effect of Ti-Rich TiN Film on Thermal Stability of $\text{Ge}_2\text{Sb}_2\text{Te}_5$ for Phase Change Memory,” *ECS Journal of Solid State Science and Technology* **5**(5), 245 (2016).
41. D. Gao, B. Liu, and Z. Xu, *et al.*, “Thermal transport properties of strontium intercalated titanium diselenide,” in *AIP Conference Proceedings*, Volume 1536, No. 1, 373–374245 (2016).
42. R. Chen, Z. Fang, and C. Perez, *et al.*, “Non-volatile electrically programmable integrated photonics with a 5-bit operation,” *Nat. Commun.* **14**(1), 3465 (2023).
43. K. Aryana, J. T. Gaskins, and J. Nag, *et al.*, “Interface controlled thermal resistances of ultra-thin chalcogenide-based phase change memory devices,” *Nat. Commun.* **12**(1), 774 (2021).
44. J. Zhao, J. Hui, and Z. Ye, *et al.*, “Exploring “no man’s land”—arrhenius crystallization of thin-film phase change material at $1\ 000\ 000\ \text{k}\ \text{s}^{-1}$ via nanocalorimetry,” *Adv. Mater. Interfaces* **9**(23), 2200429 (2022).
45. W. K. Njoroge, H.-W. Wöltgens, and M. Wuttig, “Density changes upon crystallization of $\text{ge}_2\ \text{sb}_{2.04}\ \text{te}_{4.74}$ films,” *J. Vac. Sci. Technol., A* **20**(1), 230–233 (2002).
46. T. Kato and K. Tanaka, “Electronic properties of amorphous and crystalline $\text{ge}_2\text{sb}_2\text{te}_5$ films,” *Jpn. J. Appl. Phys.* **44**(10R), 7340 (2005).
47. A. Pashinkin, A. Malkova, and M. Mikhailova, “The heat capacity of solid antimony selenide,” *Russ. J. Phys. Chem. A* **82**(6), 1035–1036 (2008).
48. K. Zeng, D.-J. Xue, and J. Tang, “Antimony selenide thin-film solar cells,” *Semicond. Sci. Technol.* **31**(6), 063001 (2016).
49. M. A. Popescu, *Non-Crystalline Chalcogenides*, vol. 8 (Springer Science & Business Media, 2001).
50. V. Gurevich, K. S. Gavrichiev, and E. Busheva, *et al.*, “Low-temperature heat capacity of antimonite sb_2s_3 (cr),” *Geochemistry International* **40**(2), 164–176 (2002).
51. T. B. Nasr, H. Maghraoui-Meherzi, and N. Kamoun-Turki, “First-principles study of electronic, thermoelectric and thermal properties of sb_2s_3 ,” *J. Alloys Compd.* **663**, 123–127 (2016).